

## Simulated Convective Lines with Leading Precipitation. Part I: Governing Dynamics

MATTHEW D. PARKER\* AND RICHARD H. JOHNSON

*Department of Atmospheric Science, Colorado State University, Fort Collins, Colorado*

(Manuscript received 3 April 2003, in final form 2 February 2004)

### ABSTRACT

This article, the first of two describing a study in which the authors used idealized numerical simulations to investigate convective lines with leading precipitation, addresses the dynamics governing the systems' structures and individual air parcels' accelerations within them. It appears that, although unconventional, systems with inflow passing through their line-leading precipitation can be stable and long lived. Lower-tropospheric inflowing air in the simulations ascends, overturns in deep updrafts, and subsequently carries its water content forward from the convective line, where it gives rise to the leading precipitation region. Although relatively strong wind shear in the middle and upper troposphere accounts for a component of the downshear acceleration, and hence overturning, of air parcels in the simulated updrafts, a mature system with leading precipitation also renders both persistent and periodic pressure anomalies that contribute just as much. Many of these accelerations, which govern the overall system structure, are largely transient and are lost when averaged over multiple convective cycles. This article explains the dynamics that govern the transient updrafts and downdrafts within the systems, including a precipitation cutoff mechanism that governs their multicellular periods.

### 1. Introduction

The importance of mesoscale convective systems (MCSs) to the agriculturally prolific central United States has long been established (e.g., Fritsch et al. 1986). However, recent work by Parker and Johnson (2000) has revealed recurring organizational modes for MCSs in this region (Fig. 1), among which are the poorly understood convective lines with leading stratiform (LS) precipitation. Parker and Johnson (2004b, hereafter PJ04) outlined a basic conceptual model for *front-fed LS (FFLS) systems*, as shown in Fig. 2, whose lower tropospheric inflow passes through a region of line-leading precipitation. They noted that these systems have heretofore received relatively little notice, even though they account for an important fraction of linear MCSs in the central United States (Parker and Johnson 2000). This paper is the first of two addressing the basic structures of FFLS systems, and the dynamics that account for and sustain them; the companion paper, Parker and Johnson (2004a), is hereafter referred to as "Part II." It is important to understand the full spectrum of organized convective systems because MCSs' organizational modes have a direct effect on their propensity to

produce large local rainfall totals and flooding (Doswell et al. 1996).

Numerical modeling techniques are desirable for attacking this problem owing to the paucity of high-resolution observations (e.g., dual-Doppler wind fields) available for in-depth case studies. FFLS systems are of themselves interesting from a numerical modeling perspective, because previously published works have documented simulations that lie roughly within the appropriate range of vertical wind shear for FFLS systems, yet in which a long-lived system failed to develop. Among such near misses are simulations by Hane (1973), Thorpe et al. (1982), Seitter and Kuo (1983), Nicholls et al. (1988), Weisman et al. (1988), and Szeto and Cho (1994). In general these systems did not produce large leading precipitation regions, even though their general structures resembled those of the FFLS systems in this publication, and were not very long lived. Hane (1973) noted that, "some rain tends to fall on the right-hand [downshear] side of the cloud [which] creates additional difficulty for the regeneration process," and Seitter and Kuo (1983) noted that, when "large amounts of liquid water were carried forward into the anvil of the storm . . . the fall of this water into the front of the storm led to excessive loading of the updraft and caused a rapid decay of the storm." Interestingly, Dudhia et al. (1987) claimed that, "no convincing example of steady convection of the pure steering-level [i.e., overturning updraft] type has yet been demonstrated in two dimensions." Some reasons for the prior failures to simulate FFLS systems may include the

\* Current affiliation: Department of Geosciences, University of Nebraska at Lincoln, Lincoln, Nebraska.

Corresponding author address: Dr. Matthew Parker, 214 Bessey Hall, University of Nebraska at Lincoln, Lincoln, NE 68588-0340.  
E-mail: mparker@papagayo.unl.edu

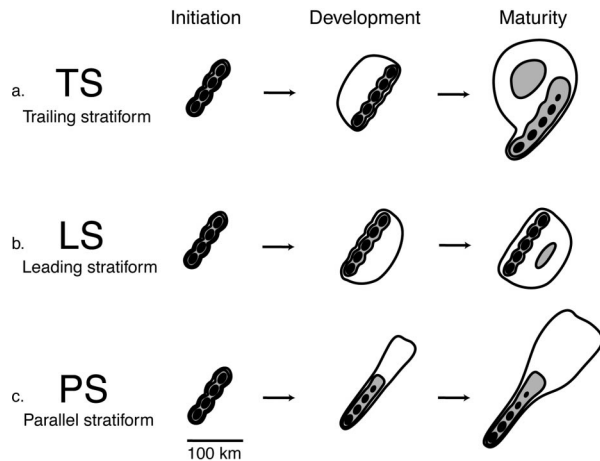


FIG. 1. Schematic reflectivity drawing of idealized life cycles for three linear MCS archetypes from Parker and Johnson (2000): (a) leading-line TS, (b) convective line with LS, and (c) convective line with parallel stratiform (PS). Approximate time interval between phases: for TS 3–4 h; for LS 2–3 h; for PS 2–3 h. Levels of shading roughly correspond to 20, 40, and 50 dBZ.

manner in which those scientists initiated the convection (i.e., using a bubble instead of a cold pool), their exclusion of the ice phase, and/or the possibility that the temperature and humidity profiles in their environments were not appropriate for the destabilization mechanism that helped to maintain the simulated systems in the present study (Part II).

As mentioned by PJ04, the history of squall line and MCS research is grounded largely in a rich sequence of papers describing convective lines with trailing stratiform (TS) precipitation. Among the numerous papers addressing TS systems, authors such as Newton and Fankhauser (1964), Houze and Rappaport (1984), Kessinger et al. (1987), Fankhauser et al. (1992), Grady and Verlinde (1997), and Nachamkin et al. (2000) studied systems with at least some FFLS characteristics. These, along with consideration of another well-observed FFLS case, led PJ04 to propose the basic conceptual model for the kinematic and reflectivity structures of FFLS systems in Fig. 2, whose salient features include a mean overturning updraft and an upper-tropospheric zone of rear-to-front outflow that feeds the leading precipitation region. With idealized numerical simulations that compared various kinds of LS and TS systems, PJ04 pointed to the importance of the lower-tropospheric and deep-layer wind shear vectors in helping to determine quasi-2D systems' organizational modes. However, although they produced reasonable FFLS simulations, they were unable to discuss the systems' details.

In addition to the above studies, other authors have used high-resolution, idealized numerical simulations to advance the dynamical understanding of convective lines. For example, Yang and Houze (1995) used idealized simulations to suggest that the periodic behavior of multicellular squall lines is attributable to gravity

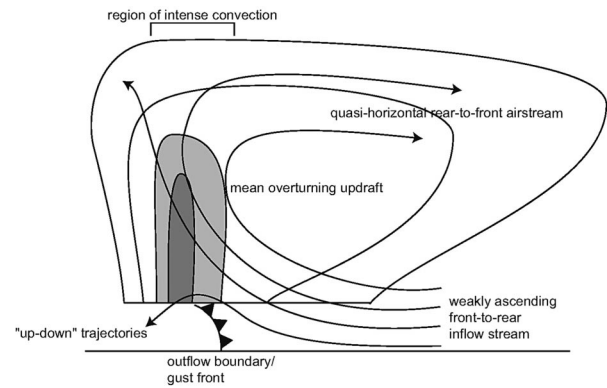


FIG. 2. Conceptual model of a front-fed convective line with leading precipitation from PJ04, viewed in a vertical cross section oriented perpendicular to the convective line and parallel to its motion.

waves forced by a quasi-steady gust front updraft. In contrast, Fovell and Tan (1998) simulated an unsteady gust front updraft and attributed the convection's periodic behavior to a cutoff mechanism induced by the buoyant updrafts themselves. The simulation results of Lin et al. (1998) and Lin and Joyce (2001) led them to suggest that the middle-tropospheric flow controls the speed at which the active cells are advected away from the gust front updraft, and therefore the period with which new convection can be generated. This paper describes a similar effort to learn about convective dynamics by analyzing high-resolution numerical simulations.

In the following section we outline the setup of the numerical model and describe our analysis techniques. Thereafter, section 3 describes simulated FFLS systems' temporally averaged features, and section 4 describes the temporally varying dynamics that account for those features. We conclude this paper with a synthesis of FFLS systems' mean and transient behavior in section 5. Part II then resumes with discussion of the mechanism that enables the simulated systems to survive inflow that passes through their preline precipitation, as well as the evolution of FFLS systems to other modes and the sensitivities of these processes.

## 2. Methods

### a. Numerical model

This paper makes use of idealized numerical simulations to describe the basic evolutions and dynamics of front-fed convective lines with leading precipitation. This work incorporated both 2D and 3D simulations using version 4.5.2 of the Advanced Regional Prediction System (ARPS), a fully compressible nonhydrostatic model developed by the Center for Analysis and Prediction of Storms (CAPS) and the University of Oklahoma. The dynamical framework of the ARPS was described by Xue et al. (1995, 2000, 2001).

The basic 2D configuration of the model for this study

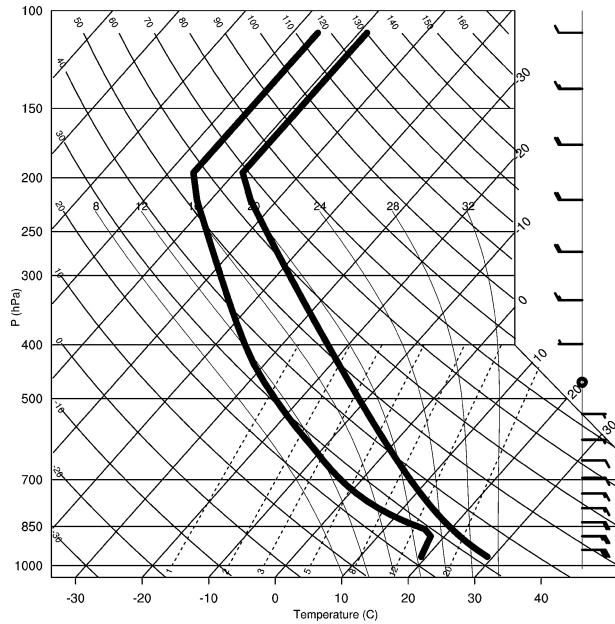


FIG. 3. Skew  $T$ - $\ln p$  diagram of the mean MCS temperature and humidity soundings used in this study, and base-state  $u$ -wind profile: full barb =  $5 \text{ m s}^{-1}$ ; half barb =  $2.5 \text{ m s}^{-1}$ . See Part II for graphical depiction of  $u$  wind vs height. Bulk thermodynamic variables for this sounding are given in Table 1.

was described by PJ04. The configuration of the 3D simulations was identical to that for the 2D simulations, with the following exceptions. The across-line ( $\hat{x}$ ) and vertical ( $\hat{z}$ ) dimensions remained 600 and 18 km, respectively, as described by PJ04, but the along-line ( $\hat{y}$ ) dimension was 300 km. The large along-line extent allowed individual convective cells to develop at spacings that were intrinsic to the problem rather than those imposed by a small domain's along-line period, and permitted the modeled convective cells to move and interact with one another more naturally, much as real-world convective cells would when part of a long, quasi-2D line. It also increased the number of convective cells on the domain at any time, allowing computation of a greater variety of air parcel trajectories. In order to explicitly simulate convective clouds on the domain, the 3D simulations had grid spacings of 2 km. The vertical grid in the 3D model was stretched, with an averaged spacing of 643 m, ranging from 400 m in the lowest 2 km of the domain to 780 m in the stratosphere. The simulations incorporated implicit differencing in  $\hat{z}$  and used a large time step of 6 s and a small (acoustic) time step of 3 s.

The 3D simulations incorporated a periodic boundary condition on the northern and southern edges of the domain (at the line's ends) in order to simulate quasi-2D convective lines. As described by PJ04, the central regions of long but finite-length simulated 3D convective lines behave much like 2D and periodic 3D lines, especially when the environmental wind profile is nearly 2D and convection is initiated with a long linear trigger. Open (rather than periodic)  $\hat{y}$  boundary conditions might

TABLE 1. Bulk thermodynamic variables for the analytic mean MCS sounding. Parcel indices are computed using an unmixed surface air parcel.

Thermodynamic parameter	Value
Lifting condensation level (hPa)	840
Level of free convection (hPa)	795
Convective available potential energy ( $\text{J kg}^{-1}$ )	2577
Convective inhibition ( $\text{J kg}^{-1}$ )	-34
Lifted index (K)	-8.4
Precipitable water (cm)	3.20

be important because they remove the quasi-2D constraint upon gravity wave dispersion. However, as discussed by PJ04, this constraint likely exists to some degree in the middle sections of long quasi-2D convective lines, in addition to which, tests revealed that the simulated convection's structure and evolution were not affected much by changing the  $\hat{y}$  boundary condition.

The control simulations did not include Coriolis accelerations or radiative effects. Several sensitivity tests, in which the Coriolis parameter ( $f$ ) was set to  $1 \times 10^{-4} \text{ s}^{-1}$  (a typical midlatitude value) revealed that the inclusion of planetary rotation had little discernable effect on the simulations during their first 6 h (the focus for the analyses in this publication). The results of the simulations with Coriolis accelerations are not described in the text. In like manner, a sensitivity test using an infrared radiation parameterization scheme revealed few appreciable differences during the first 6 h of the simulation.

The model had a horizontally homogeneous initial condition, which was defined by a single base-state sounding as described by PJ04 and shown in Fig. 3. The bulk thermodynamic variables that describe the mean MCS sounding are summarized in Table 1, and were discussed by PJ04. The base-state wind profile for the front-fed LS system control runs was taken as the average wind profile of four archetypal front-fed LS systems (which were among the population of LS MCSs summarized by Parker and Johnson 2000). For simplicity, the wind profile was reduced to anchor points, and varied linearly between the values at the anchor points. The  $u$ -wind values for the control run are plotted in Fig. 3. This profile is truer to observed FFLS systems than the simplistic profiles that PJ04 used for their sensitivity tests. The control run's initial state was 2D, and included no  $v$  wind. Sensitivity tests indicated that the inclusion of a realistic  $v$  wind did not substantially affect the structure or evolution of the periodic 3D simulations.

The method of convective initiation was identical to that described by PJ04, except that the infinitely long, 2-km-deep cold box had a constant buoyancy of  $-0.1 \text{ m s}^{-2}$  (which corresponds to a potential temperature perturbation of  $-3.2 \text{ K}$  in the base-state sounding). This was the minimal cold pool strength that reliably initiated a long-lived convective system. Because the first round

of simulated convection in the model produced much colder surface outflow, the later simulated convection was fairly independent of the initial trigger. For all of the 3D simulations, the cold box included small ( $\leq 0.1$  K) random fluctuations in order to help 3D structures develop and amplify. While the initial convection was fairly 2D, after 2 h of simulation the convective lines were cellular and remained 3D for the duration of the simulations.

### b. Analysis techniques

As described by PJ04, we carried out analyses of the components of the pressure field, defined as follows. The pressure perturbations can be diagnosed using the method presented by Wilhelmson and Ogura (1972). Separating into buoyant and dynamic parts ( $p' = p'_B + p'_D$ ), following Rotunno and Klemp (1982), yields

$$\nabla^2 p'_B = \frac{\partial}{\partial z}(\rho_o B); \quad (1)$$

$$\nabla^2 p'_D = -\rho_o \left[ \underbrace{\left( \frac{\partial u}{\partial x} \right)^2 + \left( \frac{\partial v}{\partial y} \right)^2 + \left( \frac{\partial w}{\partial z} \right)^2 - w^2 \frac{\partial^2}{\partial z^2} (\ln \rho_o)}_{\text{extension terms}} \right] - 2\rho_o \underbrace{\left( \frac{\partial v}{\partial x} \frac{\partial u}{\partial y} + \frac{\partial u}{\partial z} \frac{\partial w}{\partial x} + \frac{\partial v}{\partial z} \frac{\partial w}{\partial y} \right)}_{\text{shear terms}}; \quad (2)$$

wherein  $B$  is the buoyancy and all other variables have their conventional meanings; the terms in (2) are labeled following Klemp (1987). In the base-state environment with a mean  $u$ -wind profile, the linear part of (2) is

$$\nabla^2 p'_{DL} = -2\rho_o \frac{du_o}{dz} \frac{\partial w}{\partial x}, \quad (3)$$

which is a shear term. The remainder of  $p'_D - p'_{DL}$  is the nonlinear part of the dynamic pressure perturbation  $p'_{DNL}$ . In addition to the aforementioned authors, others (e.g., Schlesinger 1980; Cai and Wakimoto 2001) have also made use of these and similar formulations in analyzing convective dynamics.

In order to make the discussions and labeling simpler, this publication employs abbreviated names for the terms in the decomposed momentum equation, as shown by brackets below. For anelastic, inviscid, irrotational flow, the equation for motion is

$$\frac{D\mathbf{u}}{Dt} = -\underbrace{\frac{1}{\rho_o} \nabla p'}_{\text{ACC}} - \mathbf{g} \left( \frac{\rho'}{\rho_o} \right). \quad (4)$$

By applying  $p' = p'_B + p'_{DL} + p'_{DNL}$ , regrouping the terms, and explicitly writing the hydrometeor contribution to density, (4) becomes

$$\frac{D\mathbf{u}}{Dt} = -\frac{1}{\rho_o} \nabla p'_B - \underbrace{\mathbf{g} \left( \frac{\rho'_{\text{gas}}}{\rho_o} \right)}_{\text{BUOY}} - \underbrace{\mathbf{g} q_h}_{\text{DRAG}} - \frac{1}{\rho_o} \nabla p'_{DL} - \frac{1}{\rho_o} \nabla p'_{DNL}, \quad (5)$$

ACCBL

wherein  $\rho'_{\text{gas}}$  is the density perturbation attributable to the gaseous constituents and  $q_h$  is the total hydrometeor mixing ratio. The abbreviations in (4) and (5) appear throughout this article.

To facilitate analysis of air parcels, the model computed particle trajectories during the simulations. Because the background total water content in the middle and upper troposphere is quite low, air parcels with high water content must be transported forward from the convective line in order for leading stratiform precipitation to develop, or rearward in order for trailing stratiform precipitation to develop. Both temporally averaged fields and parcel trajectories (see, e.g., section 4) confirm that the water in the leading precipitation regions of the present simulations is attributable primarily to air parcels that have ascended in the convective updrafts. Plus or minus gains and losses from vertical divergence in the precipitation flux, air parcels from the lower troposphere carry with them their comparatively high total water contents. Therefore, the most suitable way to analyze the dynamics that generate a leading or trailing stratiform precipitation region is to analyze the dynamics that affect the velocities of individual parcels as they pass through the convective region.

Accordingly, it is worthwhile briefly to describe simple cold pool, updraft, and wind shear configurations that account for components of the perturbed pressure field, in order to provide points of reference for the ensuing discussions. In the limit of 1D ( $\nabla p'_B = \partial p'_B / \partial z$ ), (1) represents the hydrostatic equation and is consistent with a surface cold pool having comparatively higher surface pressure than the undisturbed environment (Fig. 4a). Additionally, because  $\partial B / \partial z > 0$  in the upper parts of realistic cold pools, simple consideration of (1) also implies minimized pressure in their upper reaches. Because, in most circumstances, the  $p'_B$  field has horizontal structure and is not hydrostatic, both (a) horizontal accelerations occur, and (b)  $p'_B$  is insufficient to oppose the negative buoyancy in the cold pool, such that the dense air descends (as depicted by the dashed arrow in Fig. 4a). As a result, the accelerations due to buoyancy and  $p'_B$ , as shown in Fig. 4a, generate a local circulation that renders relatively high dynamic pressure near and ahead of the cold pool's gust front and relatively low pressure in the cold pool's head (Fig. 4b), owing to low-level convergence ahead of the cold pool's leading edge [extension terms in Eq. (2)] and to local rotation in the cold pool's head [shear terms in Eq. (2)]. Following (3), an updraft in a mean-sheared environment exhibits relatively high pressure on its upshear side and relatively

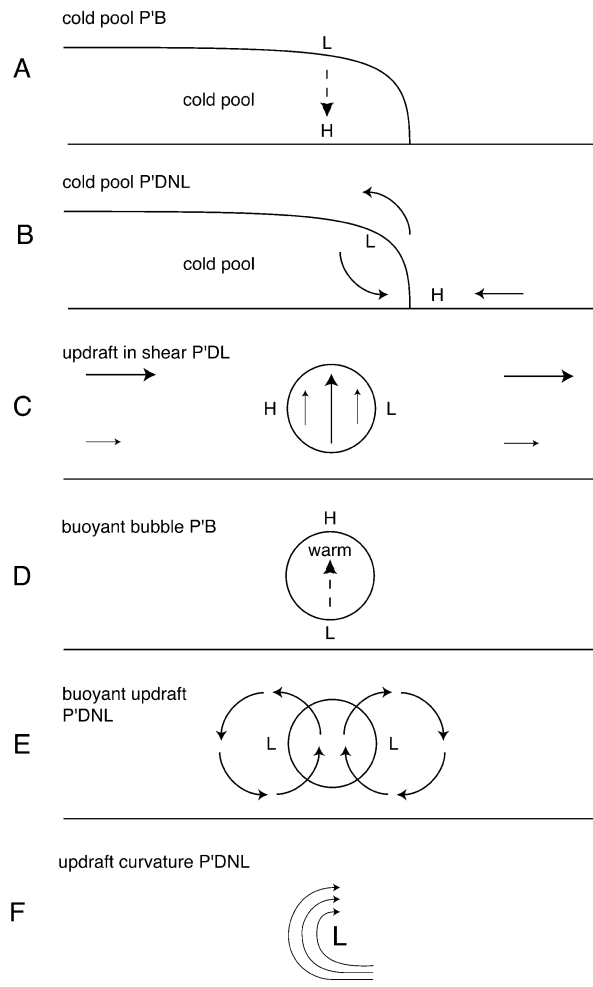


FIG. 4. Schematic depiction of simple cold pool, updraft, and wind shear configurations that account for components of the perturbed pressure field. Wind streamlines are depicted as solid arrows, buoyant accelerations are depicted as dashed arrows, and pressure maxima and minima are denoted by H and L, respectively. Subfigures (a)–(f) are explained in the text. Sizes and magnitudes are not necessarily scaled quantitatively.

low pressure on its downshear side (Fig. 4c). Additionally, (1) implies that a bubble of buoyant air exhibits relatively high pressure above and relatively low pressure below its center (Fig. 4d). The  $p'_b$  field associated with a buoyant updraft (Fig. 4d) will therefore cause divergence above the updraft, convergence below the updraft, and subsidence to the sides of the updraft, rendering a vortical circulation such as depicted by the arrows in Fig. 4e, which is consistent with locally minimized pressure via the shear terms in (2). Although it is merely a refinement to the  $p'_{DNL}$  field associated with a simple buoyant updraft (Fig. 4e), for strongly curved flow fields (in this case updrafts), the pressure minimum on the side nearer to the axis of rotation has an increased magnitude, while the pressure minimum on the side farther from the axis of rotation has a decreased magnitude (Fig. 4f).

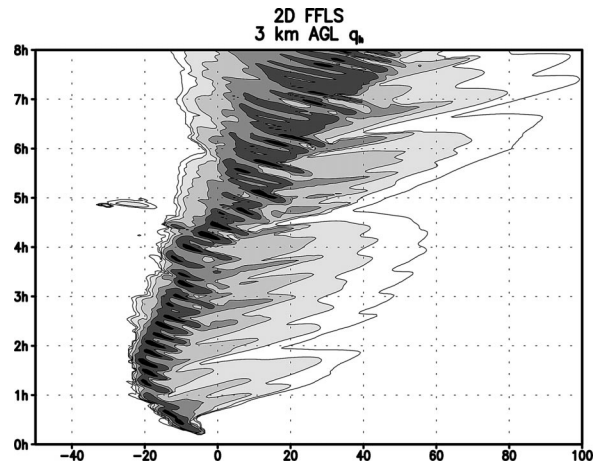


FIG. 5. Hovmöller diagram depicting 3-km-AGL hydrometeor mixing ratio ( $t = 0$ –8 h) for 2D FFLS simulation. Levels of shading are 0.005, 0.02, 0.08, 0.32, 1.28, and 5.12  $\text{g kg}^{-1}$ .

### 3. Quasi-stable structures

In a 2D simulation using the control sounding and base-state wind profile (Fig. 3), a long-lived front-fed convective line with leading precipitation occurred (Fig. 5), many aspects of which are quite similar to the FFLS simulations described by PJ04, whose conclusions will by and large not be repeated here. As can be seen in Fig. 5, the leading precipitation region developed with time throughout the first 4 h of the simulation. Deep convection was continually initiated above the surface cold pool in the vicinity of its outflow boundary and, as can be inferred from Fig. 6, each updraft pulse of the multicellular system contributed a patch of enhanced water content to the plume of line-leading hydrometeors. The persistent periodic phase of the FFLS system shown in Fig. 6 is of interest because it is *quasi stable*; in other words, despite the chaotic details of the evolving flow, similar behaviors continue to occur periodically over an extended range of time.<sup>1</sup>

On average, during the mature phase of the 2D FFLS system, air below  $\sim 6$  km AGL flows westward and passes through a preline region of cloud and precipitation on its way to the convective zone (Fig. 7). Some of this inflowing air ascends and feeds deep convective updrafts while the remainder does not attain a level of free convection and instead passes through the line's mean position, in some cases being cooled and contributing to the surface cold pool (Fig. 7). Notably, it is not clear from Fig. 7 that air below  $\approx 4.5$  km AGL ever participates in the deep convective updrafts. This is a result of averaging; time-dependent air parcel trajectories such as A–a in Fig. 8 do ascend in deep updrafts, but other lower-tropospheric inflowing parcels like B–b and C–c in Fig. 8 do not. Indeed, the magnitude of

<sup>1</sup> Such a condition has also been referred to as “quasi equilibrium” and “statistically steady,” for example, by Fovell and Ogura (1988).

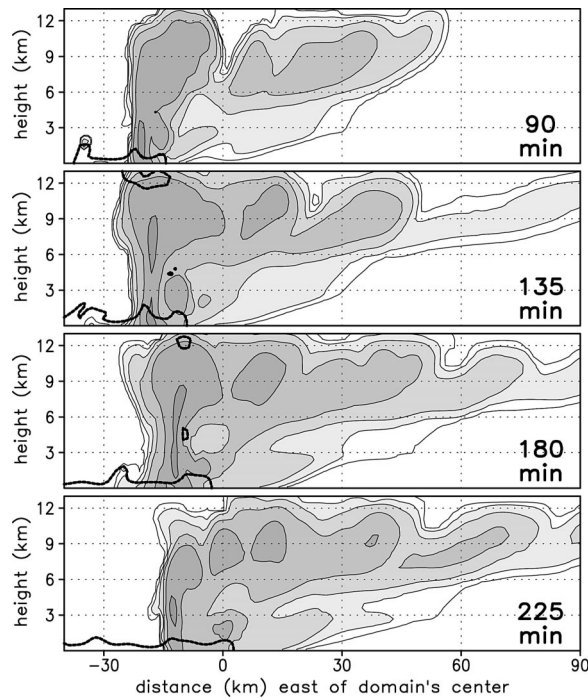


FIG. 6. Total hydrometeor mixing ratio ( $q_h$ ) and cold pool location for selected times during the 2D FFLS system's quasi-stable period;  $q_h$  thinly contoured and shaded at 0.005, 0.02, 0.08, 0.32, 1.28, and 5.12  $\text{g kg}^{-1}$ ; general cold pool position indicated by  $\theta' = -4$  K isopleths (thick contours).

$w$  in the convective region after temporal averaging (Fig. 7) is quite small below 5 km AGL, because this is a zone in which both updrafts (i.e., trajectories A–a and E–e) and downdrafts (i.e., trajectories B–b, C–c, and D–d) are fed by both lower- (i.e., A–a, B–b, and C–c) and middle- (i.e., D–d and E–e) tropospheric inflow. Almost all of the updraft trajectories overturn (e.g., A–a and E–e in Fig. 8) and are detrained with significant westerly velocities (i.e., above 7 km AGL in Fig. 7), carrying at least some of their water content with them and contributing to a persistent leading precipitation region (i.e., east of  $x = 0$  km in Fig. 7). The mean flow in the middle and upper troposphere to the west of the convective region is weak, having been decelerated. A few air parcels, such as F–f in Fig. 8, are entrained into the deep convection or cross over its mean position. However, an analysis of the mass fluxes through the convective region (not shown) revealed that the environmental air above 7 km AGL on the system's upshear side contributes relatively little to the mass outflux east of the convective updraft. The predominant flow branch is an overturning updraft that is fed by both the lower- and middle-tropospheric inflow.

Although it is not practical to prepare individual cross sections for the 3D simulations like those in Fig. 6, the plan views of mean tropospheric  $q_h$  in Fig. 9 reveal that the periodic 3D FFLS simulation also exhibits a quasi-stable behavior. In particular, a line of healthy convec-

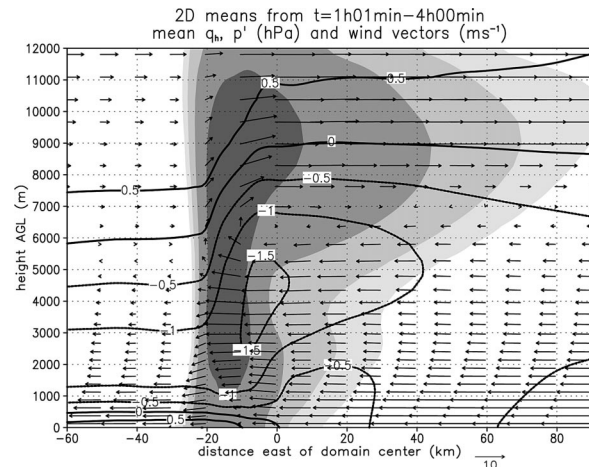


FIG. 7. Mean total hydrometeor mixing ratio (levels of shading are 0.02, 0.08, 0.32, and 1.28  $\text{g kg}^{-1}$ ), pressure perturbation (contours, hPa), and wind vectors ( $\text{m s}^{-1}$ , scaled as shown) for the 2D FFLS simulation.

tion persists, comprising individual convective cells that temporally develop, mature, and decay. Reassuringly, despite the idealized nature of the simulation and the constraint of  $\hat{y}$  periodicity, the convective line “segments” shown in Fig. 9 are similar to the reflectivity images presented by Parker and Johnson (2000, e.g., their Fig. 6). The periodic 3D system is on average quasi-2D, evidence for which includes the visually obvious slab symmetry of the structures in Fig. 9, the strong similarity of the along-line means in Fig. 10 to the temporal means from the 2D simulation in Fig. 7, and the strong similarity of the  $x$ – $z$  cross section of trajectories from the periodic 3D simulation (Fig. 11) to those from the 2D simulation (Fig. 8).

The mean fields in the 2D simulation (Fig. 7) are slightly more perturbed than those in the periodic 3D simulation (Fig. 10), which is to be expected given that

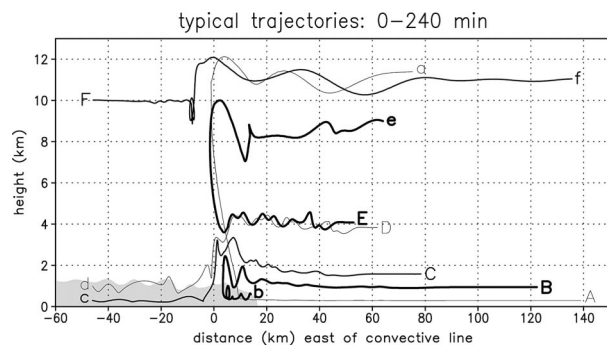


FIG. 8. Four-hour parcel trajectories typifying commonly observed airstreams for the 2D FFLS simulation. Parcels' initial positions (at  $t = 0$  min) are indicated by capital letters. Parcels' final positions (at  $t = 240$  min) are indicated by lower-case letters. Averaged  $\theta' < -2$  K are shaded to indicate the mean position of the surface cold pool during the time period. The trajectories' thicknesses vary in order to assist in differentiating them. The thicknesses have no additional meaning.

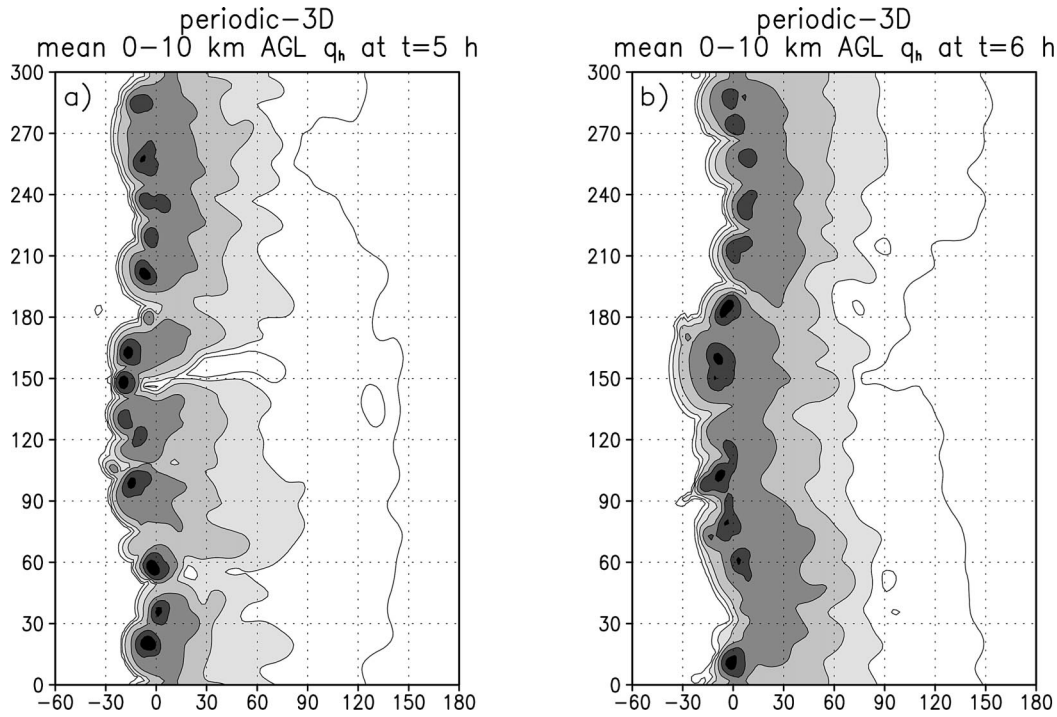


FIG. 9. Mean hydrometeor mixing ratio from 0–10 km AGL for periodic 3D FFLS simulation: (a) at  $t = 5$  h; (b) at  $t = 6$  h. Levels of shading are 0.005, 0.02, 0.08, 0.32, 1.28, and  $5.12 \text{ g kg}^{-1}$ .

the temporally averaged areal coverage of convection in the 3D simulation is somewhat less than in the 2D simulation owing to the spacing of its isolated convective cells (as seen in Fig. 9). However, the shapes of the  $q_h$ ,  $p'$ , and wind fields correspond quite well between the 2D and periodic 3D systems, and the logic of the physical processes that links them together is unchanged. Of major importance is that, not only are the averaged fields similar, but the trajectories computed in

the temporally evolving 3D flow field are quasi-2D and correspond quite well to those from the 2D simulation; air parcels' line-parallel motions are minimal (Fig. 11), such that, to a very high order, their basic paths can be described in the  $x$ - $z$  plane. In the  $x$ - $z$  plane, the 3D trajectories (Fig. 11) reveal updrafts that are fed by both lower- (e.g., trajectories 3, 8, and 9) and middle- (e.g., trajectories 2 and 6) tropospheric inflow, much like trajectories A–a and E–e in Fig. 8, as well as inflowing lower- and middle-tropospheric air parcels that cross the line's position (e.g., trajectories 1, 4, 5, and 7) and often feed the surface cold pool, much like trajectories B–b, C–c, and D–d in Fig. 8. Although the discussion in section 4 emphasizes the importance of transient accelerations and will point out differences between the transient components of the 2D and periodic 3D simulations, the present analysis also shows that, to first order, the quasi-stable characteristics and effects of the 2D and periodic 3D systems are the same. In the present study, the lack of meridional flow (Fig. 3), periodic along-line dimension, and linear initial trigger no doubt help to reinforce this similarity. Notably, numerous previous studies have also demonstrated the similarity of 2D simulations of TS systems to their 3D counterparts in the real world and in numerical models (e.g., Hane 1973; Dudhia et al. 1987; Fovell and Ogura 1988; Rotunno et al. 1988).

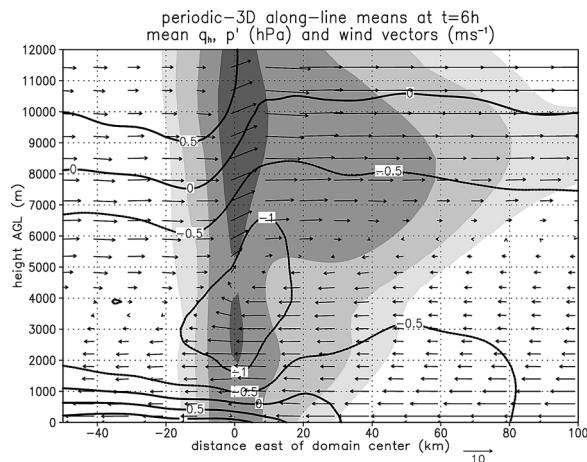


FIG. 10. Mean total hydrometeor mixing ratio (levels of shading are 0.02, 0.08, 0.32, and  $1.28 \text{ g kg}^{-1}$ ), pressure perturbation (contours, hPa), and wind vectors ( $\text{m s}^{-1}$ , scaled as shown) for periodic 3D FFLS simulation.

In the 3D simulations, the main complication to the system's quasi-2D structure is that the convective updrafts are localized, and do not resemble the infinitely

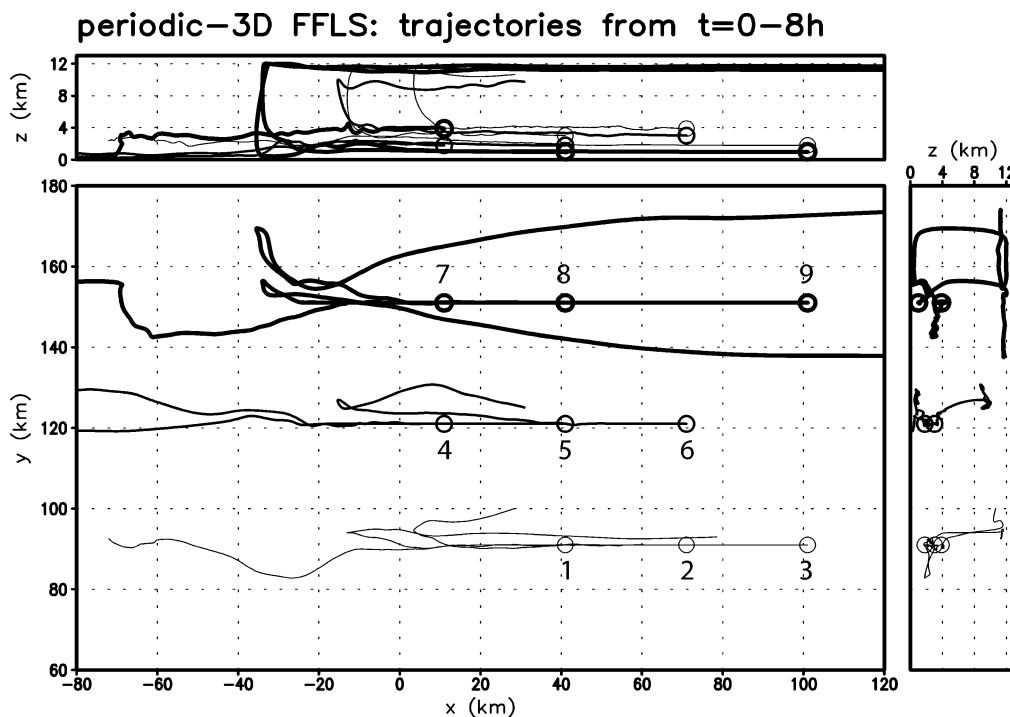


FIG. 11. “Shadow” depiction of forward trajectories computed for periodic 3D FFLS simulation. The central panel of this figure is an  $x$ - $y$  plane view of trajectory positions, the top panel is an  $x$ - $z$  cross section of trajectory positions, and the right panel is a  $z$ - $y$  cross section of positions. The trajectories begin at the  $\circ$  symbols, and are labeled for reference in the text.

long (in  $\hat{y}$ ) slabs of upward motion that occur in the 2D simulation. This has three important effects. The first is that air parcels can pass between the isolated updrafts of the periodic 3D line. Whereas in the 2D simulation the upper-tropospheric storm-relative flow must become approximately stagnant on the system’s upshear side, in 3D the upper-level flow stagnation is very local, the pressure field favors acceleration of air into the channels between active updrafts, and the mean upper-tropospheric mass flux across the convective line is approximately temporally invariant (not shown). Hence, the mean environmental flow in the 5–10-km-AGL layer on the upshear side of the convective line is much stronger in 3D than in 2D (cf. Figs. 10 and 7). The periodic 3D leading cloud and precipitation region therefore experiences slightly enhanced evaporation and sublimation as environmental flow overtakes the system. This second important effect means that the total hydrometeor load is somewhat decreased (cf. Figs. 10 and 7), and that the middle and upper troposphere is less warm (not shown). Accordingly, the quasi-static pressure minimum in the 2D case is stronger (e.g., at  $z \approx 4$  km AGL,  $x \approx -5$  km in Fig. 7), rendering comparatively stronger front-to-rear flow between roughly 3 and 6 km AGL (cf. Figs. 10 and 7), and a corresponding increase in the height of the flow reversal (from about 6 km in the periodic 3D case to about 7 km in the 2D case; cf. Figs. 10 and 7). The final important effect is that the geometry of

the  $w$  and buoyancy fields in individual 3D updrafts is different from that of the 2D updrafts. This is very important to the transient local accelerations, and is discussed in detail in section 4b. However, all caveats notwithstanding, from Figs. 10 and 11 it is clear that the periodic 3D system perturbs and overturns the environment in roughly the same way that the 2D system does.

In a mature convective system, quasi-steady perturbed pressure fields exist, which in turn induce persistent mesoscale circulations. After about 2 h of the control FFLS simulation, the mature convective system has had several prominent effects on the local winds (Fig. 12). The updrafts during this time interval occur between  $x = -15$  and  $x = 0$  km. Above 7 km AGL, dynamic and buoyant pressure maxima above the active buoyant updrafts have rendered mean storm-top divergence. Additionally, in the lowest 1.5 km AGL the buoyant pressure maximum associated both with chilling in the preline precipitation zone (discussed in detail in Part II), and with a persistent, quasi-steady surface cold pool, has produced mean westerly accelerations, which account for westerlies within the cold pool itself and for the deceleration of the easterly inflowing air to the right of  $x = 0$  km. Finally, between 2 and 6 km AGL and east of  $x = -15$  km, the wind is strongly perturbed into an easterly midlevel jet, which is largely a response to the midlevel pressure minimum that developed (and moved with the system) eastward in time (Fig. 12). This

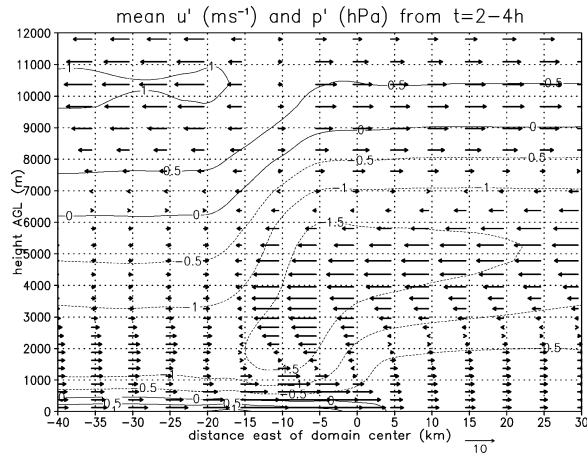


FIG. 12. Mean perturbation  $u$  wind (vectors,  $\text{m s}^{-1}$ ) and perturbation pressure (contours, hPa) for the 2D FFLS simulation from  $t = 2-4$  h. As discussed in the text, the pictured  $u'$  field is long-lived, but represents a perturbation with respect to the base state.

midlevel low is primarily from  $p'_B$  beneath the positively buoyant air exiting the convective cells and forming the leading cloud region, although  $p'_{DNL}$  owing to the curved overturning flow (as in Fig. 4f) contributes nontrivially on the downshear flank of the mean updraft's position.

Because the convective system perturbs the wind field in a way that changes the vertical shear for long periods of time (i.e., much longer than an individual convective life cycle), updrafts that occur in the local wind profile exhibit additional dynamic pressure anomalies much like those in Fig. 4c; these perturbations are diagnosed as a part of  $p'_{DNL}$  (not shown), because even though the wind perturbations are persistent they nevertheless represent deviations ( $u'$ ) from the background state. For the mature phase of the simulated FFLS system, the vertical wind shear was decreased (became more easterly) in the lowest 4 km AGL, and was increased (became more westerly) in the 4–10-km-AGL layer. From

consideration of (2), this should imply a westward ACCDNL for updrafts in the lowest 4 km, and an eastward ACCDNL for updrafts in the 4–10-km layer (Fig. 12). FFLS systems are unique because their large pressure perturbations, which are similarly found in many MCSs' stratiform regions, can in this case directly impact the inflowing air. Part II discusses how the above effects could lead to evolution or demise of a convective line with leading precipitation.

#### 4. Dynamics and kinematics

Having described the properties of the temporally averaged FFLS simulations, the paper now turns to their temporally varying parts. These transients prove to be very important to the production of an overturning updraft and leading precipitation.

##### a. A typical updraft cycle

This section documents the evolution of the components of the pressure field for a typical updraft cycle and the resultant accelerations that account for three representative air parcel trajectories from the 2D FFLS simulation. During the period of interest, approximately 2 h 40 min–3 h 18 min, an updraft occurs, followed by a suppressed period, and finally by a second updraft. As shown in Fig. 13, three air parcels (represented by  $\Delta$ ,  $\circ$ , and  $\square$ ) that approach the convective region with very similar trajectories and pass through the exact same point ( $x = -1$  km,  $z = 730$  m AGL) at different times ( $\Delta$  at about 2 h 50 min,  $\circ$  at about 2 h 52 min, and  $\square$  at about 3 h 06 min) follow markedly different trajectories through and away from the convective region. Parcel  $\Delta$  ascends in the first updraft, whereas  $\circ$  arrives about 2 min later and does not ascend. A suppressed period ensues, in which no inflowing parcels ascend in a deep updraft. Parcel  $\square$  then arrives just as the second

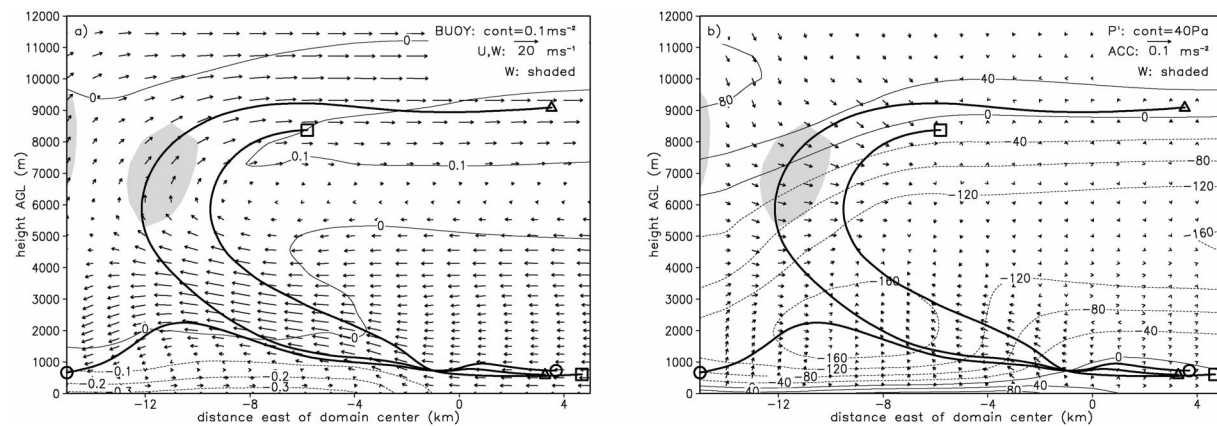


FIG. 13. Mean velocities, perturbation pressures, and acceleration terms for simulation 2D FFLS, 2 h 40 min to 3 h 18 min. (a) BUOY contoured,  $u$  and  $w$  vectors; (b)  $p'$  contoured, ACC vectors. Vertical velocity of  $5 \text{ m s}^{-1}$  is shaded. Three representative air parcel trajectories ( $\Delta$ ,  $\circ$ , and  $\square$ ) are plotted as bold curves. Contour intervals and vector scales are shown for each panel, and vary among panels. Terms are defined in section 2b.

TABLE 2. Velocities ( $\text{m s}^{-1}$ ) of the air parcels in Fig. 13 ( $\Delta$ ,  $\circ$ , and  $\square$ ) at the beginning and ending times (rounded to the nearest minute) of the averaging periods used in this section: “NC” indicates no computation of a parcel’s velocity because it was far from the region of interest.

Time	$\Delta$		$\circ$		$\square$	
	$u$ ( $\text{m s}^{-1}$ )	$w$ ( $\text{m s}^{-1}$ )	$u$ ( $\text{m s}^{-1}$ )	$w$ ( $\text{m s}^{-1}$ )	$u$ ( $\text{m s}^{-1}$ )	$w$ ( $\text{m s}^{-1}$ )
2 h 40 min	-13.2	+0.3	-12.8	+0.3	NC	NC
2 h 46 min	-4.6	+0.0	-3.9	+0.2	NC	NC
2 h 50 min	-8.7	+0.7	-5.8	-1.3	NC	NC
2 h 58 min	-17.4	+9.2	-16.3	+3.7	-10.5	-0.5
3 h 02 min	-6.6	+13.1	-14.6	+2.2	-13.5	+0.2
3 h 06 min	+13.8	+9.3	-12.2	-6.3	-8.9	+1.9
3 h 12 min	+16.7	-1.1	NC	NC	-22.4	+9.8
3 h 18 min	NC	NC	NC	NC	+13.9	+11.7

updraft forms, and ascends and overturns in it. The following discussion explains the basic accelerations that affect each parcel, and the reasons why some air parcels ascend in deep convective updrafts while others do not. Notably, by inspecting the temporally averaged fields in Fig. 13, it is impossible to determine why some air parcels ascend in the deep updrafts (i.e.,  $\Delta$  and  $\square$ ) while others do not (i.e.,  $\circ$ ). This is a key point that bears repeating: the essential dynamics that govern air parcels’ accelerations in the convective region cannot be faithfully represented by long-term temporally averaged fields.

This section assesses parcels’ accelerations by using averages over time periods of approximately 4–8 min. This is a similar tactic to that used by Fovell and Dailey (1995) and Fovell and Tan (1998), who found that they could capture multicells’ essential periodic behavior by analyzing their data at 3–8-min intervals. Although averaging over time scales even as short as 4 min removes some amount of detail, the main shape of the transient signal is still well approximated and the averaging enables the presentation of a reasonable number of figures to illustrate the discussion. During each averaging window, each plotted parcel was predominantly being accelerated in one particular direction. Table 2 displays the  $\Delta$ ,  $\circ$ , and  $\square$  (cf. Fig. 13) parcels’ starting and ending velocities for each averaging period discussed in this section. For the sake of brevity, full-page figures are included only to illustrate key points. The remainder of the text describes the accelerations that account for the data in Table 2, but without corresponding illustrations. The entire cycle is then described and illustrated at the end of this section (interested readers could refer to Fig. 18 prior to its mention in the text).

Between 2 h 40 min and 2 h 46 min, both  $\Delta$  and  $\circ$  approach the system’s outflow boundary and gust front and are decelerated (Table 2) owing almost entirely to an eastward-directed ACCB (Fig. 14c), which arises from the combination of midlevel cooling in the preline precipitation region (discussed at length in Part II) and from the surface cold pool (much as in Fig. 4a). Notably, during this period the cold pool is not producing an active, surface-based updraft (Fig. 14a); the gust front updraft exists but is not connected to deep, free con-

vection. Remnants of the previous convective cell are evident around  $x = -15$  km, and this cell has produced a strong downdraft (west of  $x = -12$  km) and surge of westerly outflow in the cold pool (Fig. 14a). From 2 h 46 min through 2 h 50 min, a new updraft develops above the outflow boundary, and  $\Delta$  begins to be lifted and accelerated rearward by ACCB (not shown for this time period, but consistent with Fig. 15c);  $\circ$ , which is slightly farther away, is not affected much (again, not shown). Between 2 h 50 min and 2 h 58 min, both parcels are accelerated upward by the vertical gradient in  $p'_B$  near the edge of the outflow (Fig. 15c) and rearward by the horizontal pressure gradient that is mainly due to  $p'_B$  (Fig. 15c, as in Fig. 4a), but also to  $p'_{DNL}$  near the cold pool’s nose (not shown, but much as in Fig. 4b). Parcel  $\Delta$  is accelerated upward more than  $\circ$  between 2 h 50 min and 2 h 58 min because it encounters the vertical gradient in  $p'_B$  sooner, and eventually it becomes positively buoyant (Fig. 15a).

As  $\Delta$  begins to ascend rapidly in the main updraft, it is accelerated strongly eastward by the horizontal pressure gradient, which largely comprises the gradients in  $p'_{DL}$  (Fig. 16e), owing to the environmental shear (as in Fig. 4c), and in  $p'_B$  (Fig. 16c), owing to the mesoscale buoyancy field (as in Fig. 4d). Updraft parcels on the eastern side of the updraft are also accelerated downshear by the horizontal gradient in  $p'_{DNL}$  (Fig. 16d), which may be attributed to the process depicted in Fig. 4f, as well as to the perturbation wind shear described in section 3. For the time period 2 h 58 min–3 h 02 min, ACCB, ACCDNL, and ACCDL all contribute to the downshear accelerations of air in the updraft. Meanwhile, although roughly following the path originally traced out by  $\Delta$ ,  $\circ$  receives no additional net upward acceleration between 2 h 58 min and 3 h 02 min (Table 2), in part because it does not become significantly buoyant (Fig. 16a), and so it does not turn sharply upward and participate in the deep updraft.

From 3 h 02 min through 3 h 06 min the updraft is weakening, and from Fig. 17a it appears that  $\Delta$  was one of the last air parcels to join the updraft before it was separated from the inflowing airstream below 5 km AGL. Because the updraft has weakened, the magnitudes of  $p'_{DNL}$  and  $p'_{DL}$  on its flanks have also weakened

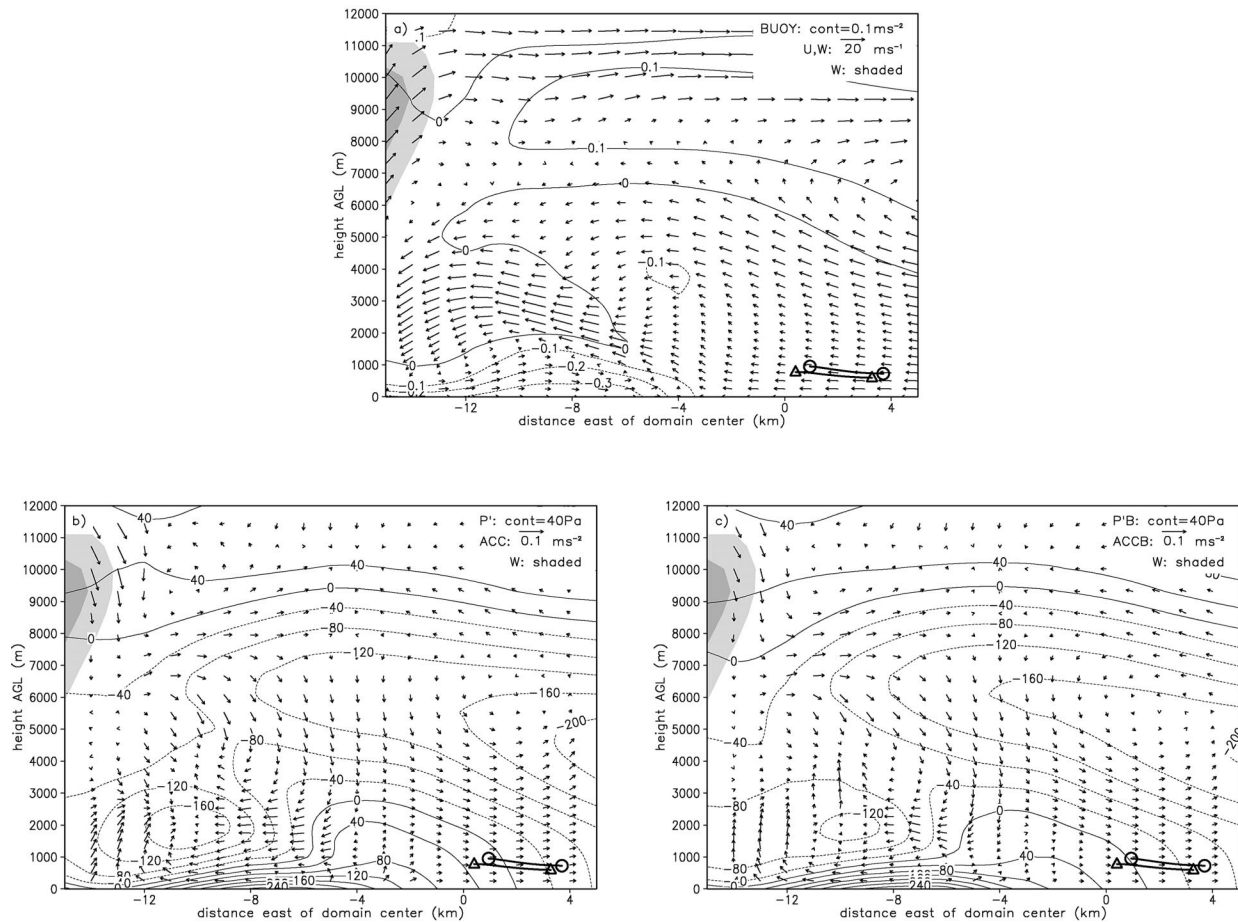


FIG. 14. Mean velocities, perturbation pressures, and acceleration terms for simulation 2D FFLS, 2 h 40 min to 2 h 46 min. (a) BUOY contoured,  $u$  and  $w$  vectors; (b)  $p'$  contoured, ACC vectors; (c)  $p'_b$  contoured, ACCB vectors. Vertical velocity shaded in all panels: levels of shading are 5 and 10  $\text{m s}^{-1}$ . Three representative air parcel trajectories ( $\Delta$ ,  $\circ$ , and  $\square$ ) are plotted to indicate their positions at the starting and ending times of the figure. Contour intervals and vector scales are shown for each panel, and vary among panels. Terms are defined in section 2b.

(cf. Figs. 17d and 17e versus Figs. 16d and 16e). Hence,  $\Delta$  is now primarily accelerated downshear by the horizontal gradient in  $p'_b$  (Fig. 17c), which is largely attributable to the mesoscale buoyancy structure (Fig. 17a, much as in Fig. 4d). In the mean time,  $\circ$  is accelerated strongly downward and begins to descend (Table 2, Fig. 17a) owing entirely to ACCB (Fig. 17c) associated with its negative buoyancy (cf. Figs. 17a and 17c). It is finally clear by 3 h 06 min that, despite their nearly identical origins and similar inflow trajectories,  $\Delta$  and  $\circ$  will have quite different fates and will not end up anywhere near one another at later times, highlighting the large degree of transience that governs accelerations in the updraft region.

Parcel  $\circ$  is accelerated downward because it begins to experience precipitation drag and loses much of its upward momentum before it is positively buoyant [i.e., before it has reached its level of free convection (LFC)]. As a result, downward accelerations owing to evaporative cooling and drag have more time to act as the

parcel moves laterally into the precipitation core. Even as  $\circ$  attains its LFC around 3 h 02 min (end of Fig. 16 and beginning of Fig. 17), it is still being accelerated downward by hydrometeor drag as it enters into the heaviest precipitation. In contrast, as  $\Delta$  enters the main precipitation core it continues to possess an appreciably positive  $w$  and has already started to become positively buoyant; from 3 h onward (about halfway along its trajectory in Fig. 16),  $\Delta$  therefore has sufficient positive buoyancy to overcome the precipitation drag, and it is accelerated upward in the main updraft.

Between 3 h 6 min and 3 h 12 min, the old updraft is completely cut off from the low-level inflow and weakens to  $w < 10 \text{ m s}^{-1}$  (not shown). During this period  $\Delta$  ends its ascent and moves with a rear-to-front storm-relative velocity, carrying its total water content with it and contributing to the leading precipitation region. Meanwhile,  $\square$  is accelerated upward and rearward during the 11 148–11 505 s window (Table 2), owing to the same processes that governed the upward and

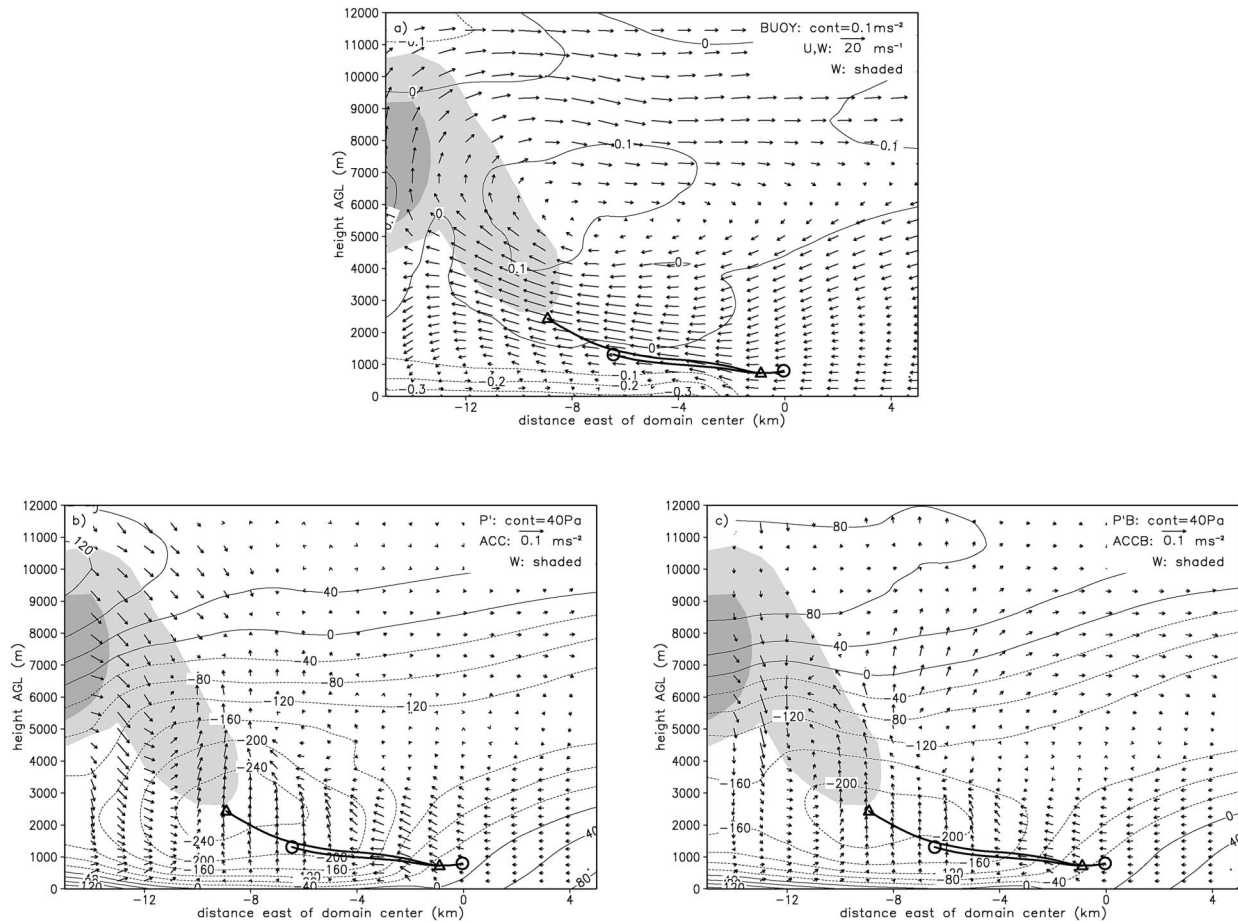


FIG. 15. Same as Fig. 14, except for simulation 2D FFLS, 2 h 50 min to 2 h 58 min.

rearward accelerations of  $\triangle$  and  $\circ$ ; eventually it attains an LFC and overturns in a new deep updraft. Notably, because the previous updraft (i.e.,  $\triangle$ 's updraft) has just produced a strong surge of outflow, a region of strong horizontal vorticity and a dynamic pressure minimum exists in the cold pool's head, as in Fig. 4b, which hinders  $\square$ 's ascent. For illustration, such an anomaly in  $p'_{DNL}$  also occurred as  $\triangle$  and  $\circ$  approached the gust front between 2 h 40 min and 2 h 46 min (not explicitly shown, but consistent with the rotor at  $x \approx -11$  km in Fig. 14a); however, in that case the parcels were not far enough west to be affected by it before it dissipated.

#### b. Conceptual model for FFLS multicells

Following the basic processes discussed above, updrafts in the FFLS simulations are alternately produced and suppressed. The local pressure and buoyancy fields follow similar cycles, and therefore the accelerations that affect air parcels in the convective region are also periodic. The general cycle is as follows. 1) Early in the lifetime of a new updraft, lifting at the edge of the cold pool is enhanced by ACCB and ACCDNL (Fig. 18a); this enhancement is largely due to a surge of out-

flow from the previous convective cycle, which strengthens the cold pool and intensifies the convergence at the gust front. Air parcels are decelerated as they approach the gust front, providing an extended period of time for the upward accelerations to impart positive  $w$  to the inflowing air parcels. Once air parcels have ascended over the outflow boundary, they are accelerated strongly rearward owing to the horizontal gradients in  $p'_{DNL}$  and  $p'_B$ . Often, the horizontal ACCB is partly attributable to a  $p'_B$  minimum below a developing cloud. 2) Air parcels are accelerated upward toward their LFCs, and this upward acceleration is largely due to the vertical gradient in  $p'_B$  at the edge of the cold pool (this is how cold pools lift air parcels). As the updraft develops at low levels, a downshear-directed ACCDL helps to provide more erect trajectories (the dashed arrow in Fig. 18a). The more erect updraft allows air to spend more time in the zone of upward acceleration, and decreases the magnitude of the minimum in  $p'_{DNL}$  over the cold pool head (the weakening of the old downdrafts also is relevant to this decrease). During the active phase of the multicell, many air parcels are lifted to their LFCs in this way (e.g.,  $\triangle$ ), participate in the main updraft, and are accelerated downshear by some com-

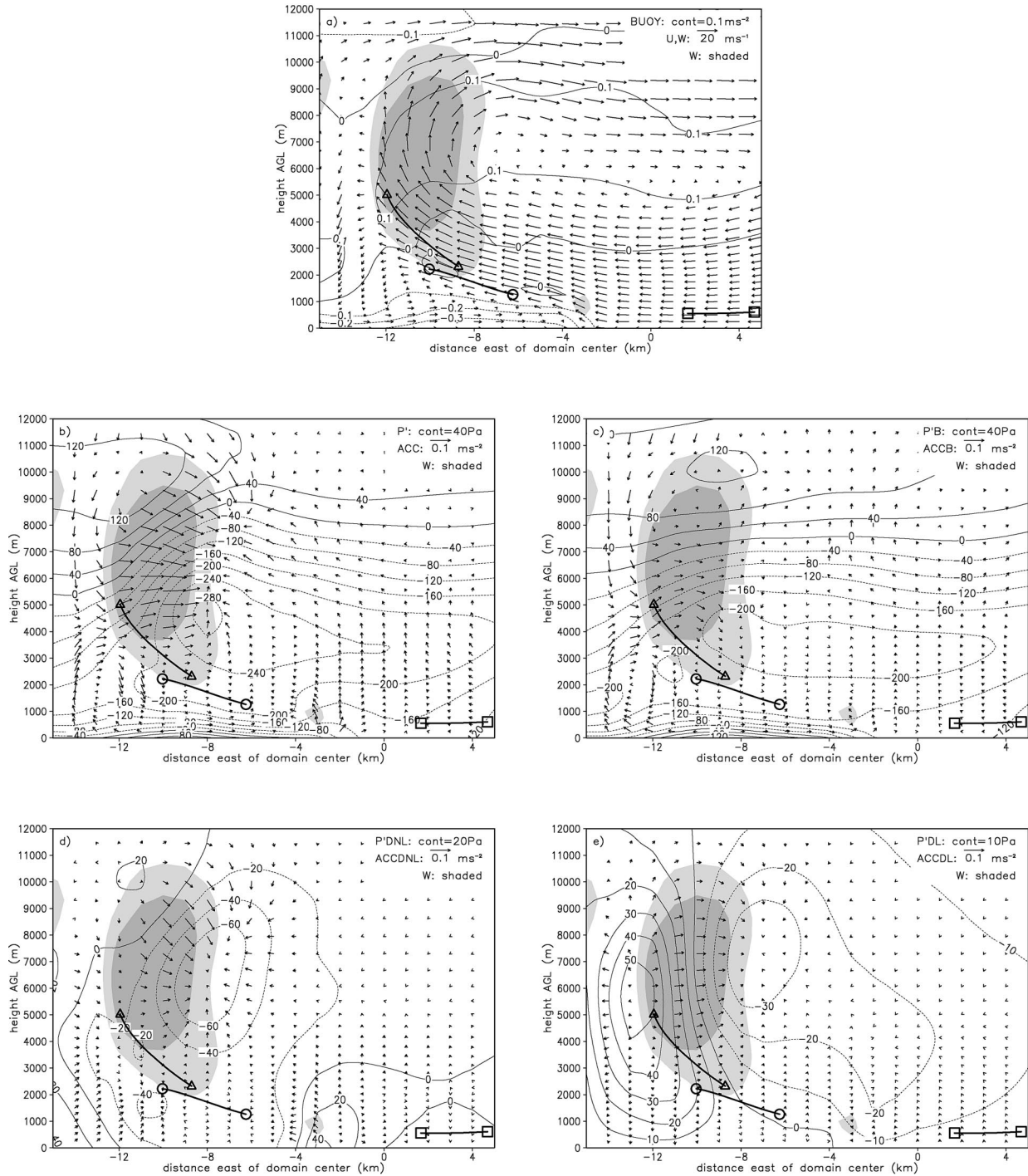


FIG. 16. Mean velocities, perturbation pressures, and acceleration terms for simulation 2D FFLS, 2 h 58 min to 3 h 2 min. (a) BUOY contoured,  $u$  and  $w$  vectors; (b)  $p'$  contoured, ACC vectors; (c)  $p'_B$  contoured, ACCB vectors; (d)  $p'_{DNL}$  contoured, ACCDNL vectors; (e)  $p'_{DL}$  contoured, ACCDL vectors. Shading, contours, vectors, and plotting of symbols are the same as Fig. 14.

combination of ACCB, ACCDNL, and ACCDL (Fig. 18b). The system deviates from the classical trailing precipitation model in that cloud and precipitation particles are carried forward from the convective updraft owing to air parcels' large net downshear accelerations. There-

fore, as the convective updraft's life span progresses, some precipitation begins to fall in advance of the updraft's position. 3) Eventually there is a point of cutoff, when inflowing air parcels experience downward accelerations owing to hydrometeor loading and evapo-

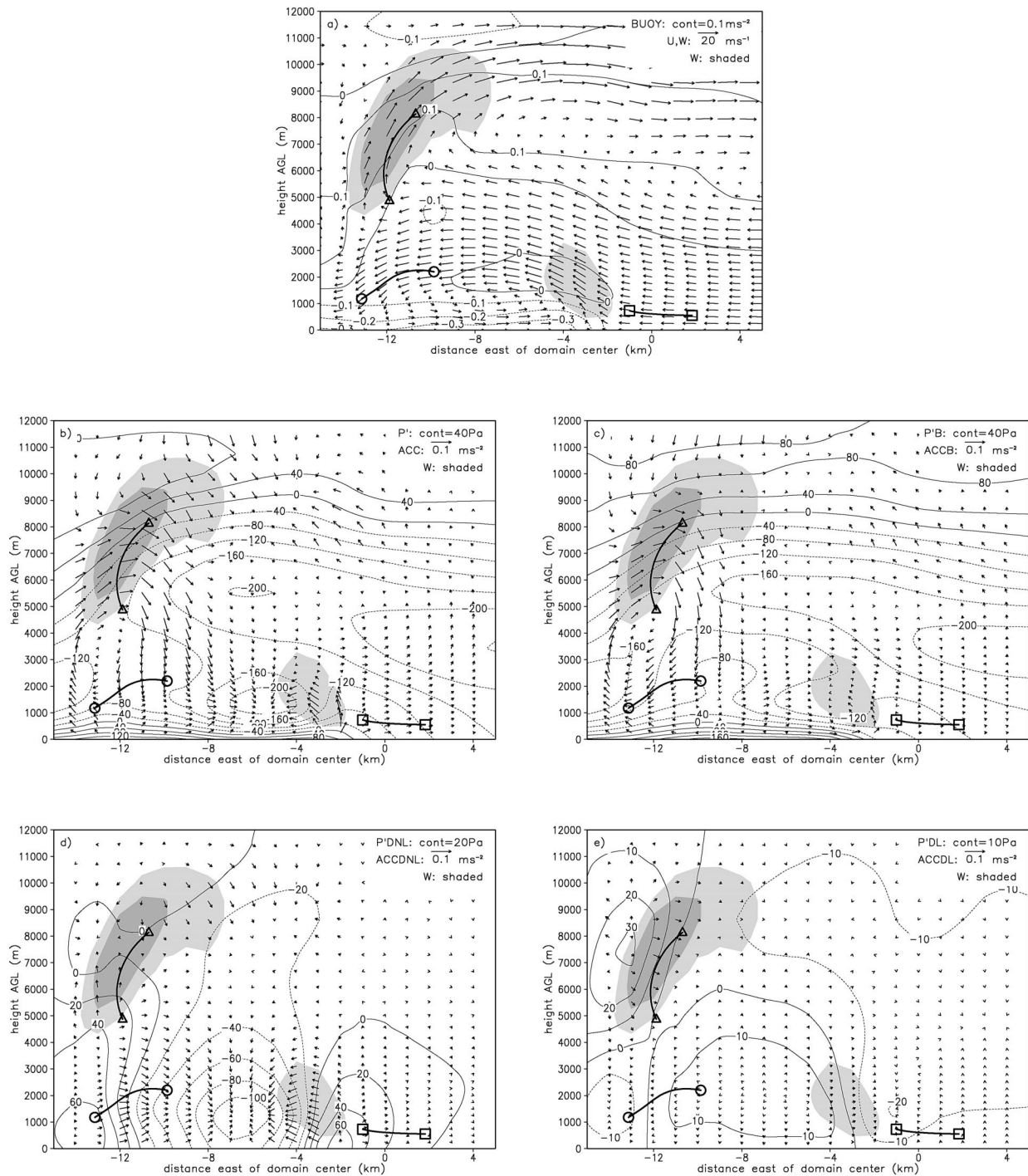


FIG. 17. Same as Fig. 16, except for simulation 2D FFLS, 3 h 2 min to 3 h 6 min.

relative cooling as they approach the updraft (e.g.,  $\odot$ ). As their vertical velocities decrease or become negative, they require longer and longer times to reach an LFC, and eventually move almost horizontally and accumulate downward acceleration until they descend (Fig. 18c). At this point, the multicell is suppressed, and no additional inflowing air parcels join the updraft. Mean-

while, the inflowing air parcels that have been strongly accelerated downward compose a downdraft and surge of outflow that strengthens the cold pool. Once the newly cutoff updraft has decayed and the precipitation curtain has dissipated sufficiently, the stage is once again set for phase 1 (i.e., for air parcel  $\square$ , or Fig. 18a).

Notably, convective systems can be multicellular ow-

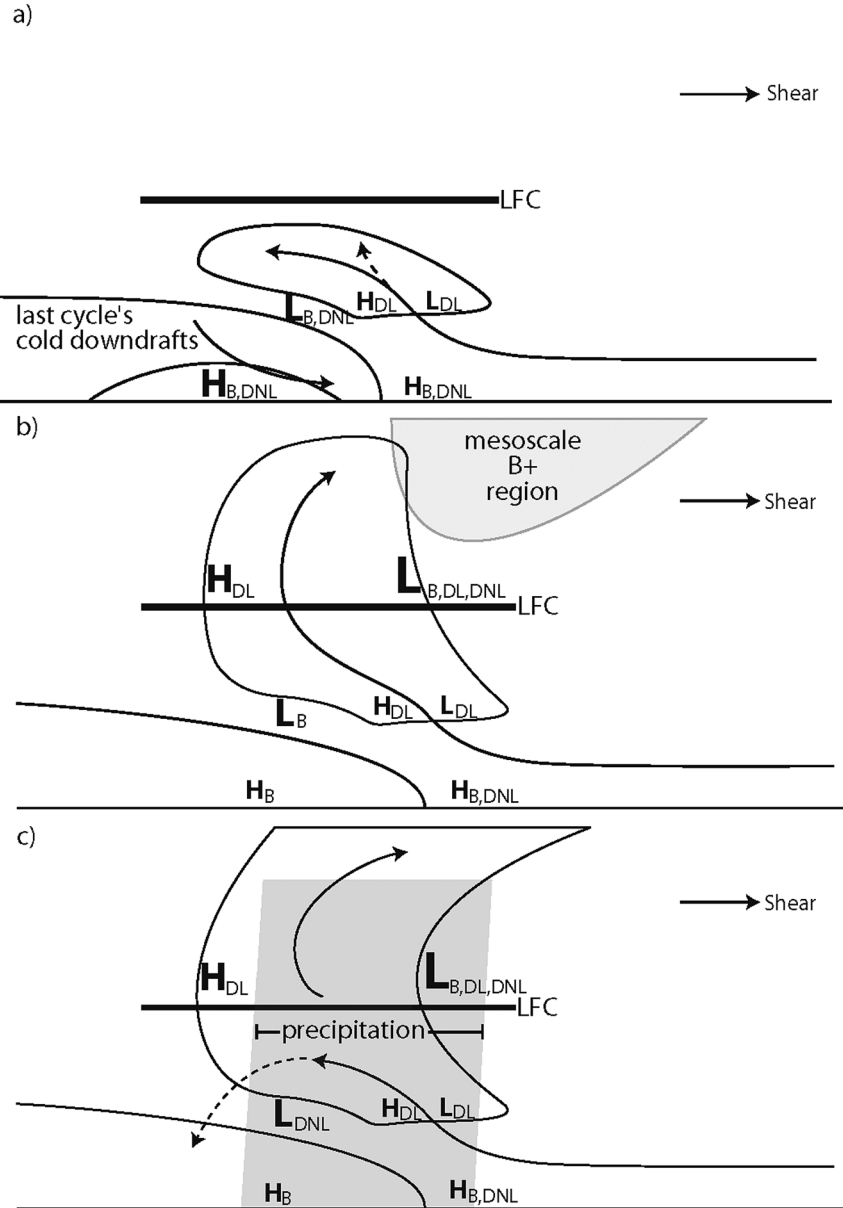


FIG. 18. Schematic depiction of the FFLS multicellular cycle. (a) Development of a fresh updraft at the outflow boundary/gust front; (b) maturation of the overturning updraft; (c) the updraft is cut off from the inflow by precipitation. The cold pool and cloud outlines are shown schematically, along with typical airstreams. The LFC and orientation of the deep tropospheric shear vector are also shown. In (b), the shaded region represents the mesoscale region of positive buoyancy associated with the line-leading cloudiness. In (c), the shaded region represents the newly developed convective precipitation cascade. Pressure maxima and minima are shown with “H” and “L” characters: their sizes indicate approximate magnitudes and their subscripts indicate the pressure components to which they are attributed. The vertical scale is expanded somewhat below the LFC and contracted somewhat above the LFC.

ing to effects other than this precipitation cutoff mechanism [e.g., the episodic entrainment mechanism proposed by Fovell and Tan (1998), discussed more later]. During experiments in which we eliminated evaporation and water loading from a mature FFLS simulation, the system took roughly 1.5 h to become completely uni-

cellular (steady). During that time as the cold pool weakened, some other mechanism, such as that described by Fovell and Tan (1998), must have accounted for the system’s multicellular behavior. However, upon reinstating water loading, the system immediately became multicellular again. In other words, the proposed pre-

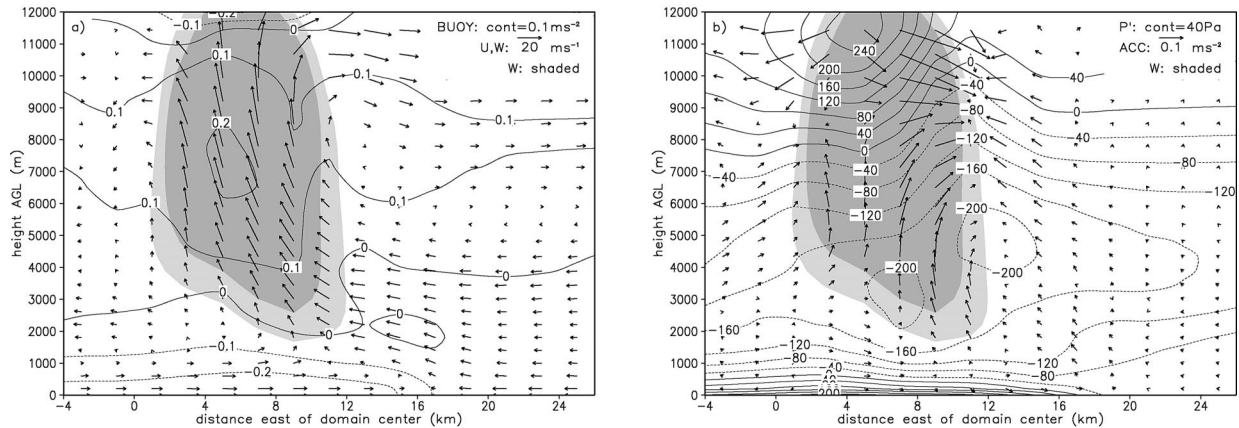


FIG. 19. Same as Fig. 13, except for simulation periodic 3D FFLS,  $y = 167$  km, 6 h.

precipitation cutoff mechanism appears to be sufficient for explaining the multicellular behavior of FFLS systems, although it is likely augmented by other contributors as well.

The simulated multicellular cycles typically have periods between about 13 and 16 min (e.g., Fig. 5), which are comparable to periods reported by other numerical multicell studies (e.g., Fovell and Ogura 1989; Fovell and Dailey 1995; Fovell and Tan 1998; Lin et al. 1998; Lin and Joyce 2001). Occasionally, longer cycles (up to approximately 30 min) occur, which correspond to a prolonged suppressed phase of the multicell system. However, the active phase of the updraft cycle almost always lasts for 8–12 min. This time scale is likely set by the thermodynamic environment and the corresponding time scale for the production of heavy convective precipitation. Interestingly, Schultz and Trapp (2003) interpreted the general movement and tilt of a cold front in terms of a similar cycle, which suggests that this conceptual model may have a somewhat broader applicability.

### c. Three-dimensional features

An important and recurring question among dynamicists and numerical modelers is the degree to which 2D simulations capture the essential physical processes of 3D systems. To this end, because the important dynamics in the updraft region are transient, it is not sufficient merely to note the similarity of the mean wind and condensate fields from the 2D and periodic 3D simulations (i.e., the similarity of Figs. 7 and 10, as was discussed in section 3). Although, it was not computationally feasible to conduct an exhaustive study of 3D trajectories, this section briefly discusses two characteristic updrafts from the periodic 3D control simulation and relates them to a foundation provided by previous studies. After 6 h of the periodic 3D simulation, the system had attained a quasi-stable FFLS configuration. This section considers a relatively weak updraft, whose

characteristics are quite similar to those discussed for the 2D simulations, and a relatively strong updraft (Fig. 19), whose characteristics are somewhat different.

Notably, the processes that govern the horizontal deceleration and upward acceleration of inflowing air parcels as they approach the gust front are very well approximated by the 2D case. Although the surface cold pool in the periodic 3D simulations is not homogeneous, it still presents a nearly north–south barrier to the inflow air, whose velocity is very nearly due easterly. As a result of the cold pool's quasi two-dimensionality, its associated  $p'_B$  and  $p'_{DNL}$  fields are also quasi 2D, and the basic air parcel accelerations in the vicinity of the outflow boundary/gust front can be explained almost entirely by resorting to the arguments used to explain the 2D case. In contrast, however, the system's updrafts are distinctly 3D. Due to the inhomogeneities in the surface cold pool, buoyant updrafts are initiated at individual points where the vertical accelerations produced by the cold pool are somewhat enhanced; this stands in contrast to the infinitely long (in  $\hat{y}$ ) updrafts produced in 2D simulations. Of course, this process also initiates updrafts at different times along the length of the line because the inhomogeneities also contribute to along-line phase shifts in the periodic process described for the 2D case. As a result of these effects, it is exceedingly uncommon for slab-like updrafts to develop in the periodic-3D simulations.

Occasionally, the periodic-3D system produces a relatively weak updraft whose shape and characteristic  $w$  closely correspond to those of the 2D simulations. These 3D updrafts resemble the 2D case (as in Figs. 13–17) in that the radius of curvature for the overturning updraft is fairly small and in that ACCB, ACCDNL, and ACCDL all contribute to parcels' downshear accelerations throughout most of the updraft. However, many of the active updrafts produced by the periodic 3D system are considerably stronger than those in the 2D case (e.g., Fig. 19a). Schlesinger (1984) discussed physical reasons for this. As in results of Soong and Ogura

(1973), Yau (1979), and Schlesinger (1984), in our 2D simulations, the  $p'_b$  field cancels about one-half to two-thirds of the buoyancy force, while in 3D, the  $p'_b$  field cancels about one-quarter to one-third of the buoyancy force. As might be anticipated, this yields a positive feedback. A greater upward ACCB in 3D yields a stronger updraft, which in turn implies a greater total condensation rate and therefore additional updraft buoyancy. Hence, most 3D updrafts have considerably larger magnitudes for  $w$ , buoyancy (e.g., Fig. 19a), and upward ACCB (not specifically shown).

In comparison to the foregoing discussion of 2D systems, the effects of increased updraft strength upon accelerations are as follows. Owing to the large and generally unopposed updraft buoyancy, ACCB within the strong 3D updraft is nearly vertical, and accounts for a comparatively small downshear acceleration (owing to the mesoscale buoyancy gradient), which is localized to the updraft's extreme downshear edge. Because the updraft is nearly vertical, and the radius of flow curvature on the downshear side is quite large, a minimum in  $p'_{DNL}$  is not specifically favored on the updraft's downshear side. Instead, a quasi-symmetrical pair of  $p'_{DNL}$  minima occur, much as in Fig. 4e. Hence, ACCDNL does not contribute any appreciable downshear acceleration to updraft air throughout most of the depth of the updraft. As might be anticipated for a stronger updraft, the downshear ACCDL is much larger (as in Fig. 4c), and accounts for almost all of the downshear accelerations imposed on air parcels that ascend in the updraft. It should be emphasized, however, that in extremely strong updrafts the parcel time scale is correspondingly shorter, so that the enhanced ACCDL has less time to act. The net result is that the updraft is erect throughout most of its depth, and the bulk of the downshear accelerations experienced by updraft air parcels occur very near the updraft's top (Fig. 19b), where the parcels are moving upward much less rapidly and where all three components of horizontal acceleration contribute in tandem.

Although more detailed analyses could certainly further differentiate 2D from 3D dynamics, much of this was already covered by Schlesinger (1984) and other authors, and will not be repeated here. Despite the apparent dissimilarity of the 2D updrafts from many of those in the periodic 3D simulations, the important overarching insights from the 2D analysis are unchanged in 3D. In particular, the 3D simulations exhibit updrafts in which the air parcels overturn owing to a combination of ACCB, ACCDNL, and ACCDL, rendering a leading precipitation zone. More importantly, the 3D simulations exhibit similar periodic behavior to the 2D simulations, and for very similar reasons (the updraft–cut-off–outflow cycle, as in Fig. 18).

#### d. Comparison to other multicellular theories

The present simulations fall within the broad population of convective lines that are generally multicellular

and exhibit periodic behavior. Yang and Houze (1995) attributed this periodic behavior to gravity waves forced by a quasi-steady gust front updraft. In the present simulations, the 2D cases do indeed evince the wavelike  $w$  and  $p'$  structures shown by Yang and Houze (e.g., their Figs. 9 and 10). However, this behavior disappears entirely in the periodic 3D simulations. It is unclear whether this result is unique to FFLS systems or simply reveals a limitation of 2D squall line studies. In contrast, Fovell and Tan (1998) simulated an unsteady gust front updraft and attributed the convection's periodic behavior to a cutoff mechanism whereby each new buoyant updraft “[sows] the seeds of its own demise” via a circulation like that implied by Figs. 4d and 4e, suppressing the gust front updraft and mixing stable environmental air into its circulation. Lin et al. (1998) and Lin and Joyce (2001) suggested that the middle tropospheric flow controls the speed at which active cells are advected away from the gust front updraft, and therefore the period with which new convection can be regenerated. It is tempting to try to relate the precipitation cutoff mechanism in the present simulations to the other cutoff mechanisms in the Fovell and Tan (1998) and Lin et al. conceptual models.

In FFLS cases with the aforementioned precipitation cutoff mechanism, the multicell's period must be strongly related to the intrinsic time scales required for the production of precipitation and cold downdrafts by convective clouds in the environment, which are complicated functions of the thermodynamic and kinematic profiles. Even so, the multicell process in the simulations is similar in spirit to those proposed by Fovell and Tan (1998) and Lin et al.; inflowing air parcels, which are spatially and temporally proximate may experience vastly different outcomes based on the evolving forcing, which in turn is a result of the convection itself. It is not clear that the updrafts are actually advected rearward as suggested by Lin et al., but the updrafts do incorporate some midlevel air with front-to-rear momentum (e.g., trajectory E in Fig. 8). In the present simulations, the inflowing air parcels move rearward through the updraft forcing and overturn, while the updraft forcing itself moves rearward with respect to the gust front. As a result, the developing updrafts and precipitation cores in the FFLS simulations still move rearward, much as in the systems studied by Fovell and Tan (1998) and Lin et al., despite the fact that the mesoscale structure of the system is quite different. However, in the present simulations, the cutoff mechanism associated with precipitation processes appears sufficient to make FFLS systems multicellular, whereas Fovell and Tan's (1998) mechanism was more difficult to detect in the analyzed FFLS systems. The fact that the overturning updraft is not situated directly above the gust front, but develops 5–10 km behind it, also makes the simulated systems very interesting in the light of the arguments for deep lifting at gust fronts advanced by Rotunno et al. (1988).

We consider the applicability of their local vorticity balance theory in Part II.

## 5. Conclusions

This work utilized the Advanced Regional Prediction System (ARPS) to simulate convective lines with leading precipitation. Using a typical environment for a mid-latitude mesoscale convective system (MCS), and a mean wind profile from archetypal cases, the model simulated a front-fed convective line with leading precipitation (an FFLS system). In both 2D and periodic 3D simulations, the FFLS systems were quasi stable, with inflowing air passing through preline precipitation and ascending in convective cells that developed periodically. In purely 2D simulations, the leading precipitation region almost entirely comprises air parcels that have ascended in the convective updrafts. In 3D simulations, however, upper-tropospheric environmental air is able to flow between convective updrafts and into the preline region.

Although this article emphasizes the importance of the transient accelerations on updraft air parcels, the systems also have important persistent effects on their mesoscale environments. Most notably, owing to a persistent pressure minimum that occurs on the line-leading side of the systems in the middle troposphere (owing to the buoyancy of the leading precipitation region and to the curvature of the overturning mean updraft), the systems contribute to the development of a front-to-rear middle-tropospheric inflow jet. In turn, this midlevel jet constitutes a decrease in the lower-tropospheric vertical wind shear and an increase in the upper-tropospheric wind shear. As a result, the mesoscale quasi-stable flow field feeds back into the transient accelerations via horizontal gradients in nonlinear part of the dynamic pressure perturbation ( $p'_{DNL}$ ), owing to ascent within the persistent perturbation wind shear.

The accelerations causing inflowing air parcels to ascend and overturn in deep convective updrafts are transient, and cannot be realistically extrapolated from temporally averaged fields. Inflowing air in the lower troposphere is periodically lifted by the buoyant and dynamic pressure field near the outflow boundary and gust front. During active phases of the multicellular system, the vertical pressure gradient lifts the air to its level of free convection (LFC); thereafter, the horizontal gradients in the buoyant, linear dynamic, and nonlinear dynamic pressure fields all contribute to the downshear accelerations of air parcels in the system updrafts. The buoyant part of the downshear-directed acceleration (ACCB) is attributable to the downshear tilt of the buoyant updrafts and to the mesoscale gradients in buoyancy associated with the FFLS system itself. The linear dynamic part of the downshear-directed acceleration (ACCDL) is attributable to the presence of an updraft in shear. The nonlinear dynamic part of the downshear-directed acceleration (ACCDNL) is attributable to the

curvature of the updraft itself and to the presence of the updraft in a profile with perturbed vertical shear. The integrated effects of these downshear accelerations are overturning updraft trajectories, with air parcels carrying their total water content into the preline region, where they begin to compose a leading precipitation region. Periodic 3D simulations of FFLS systems are somewhat more complicated than 2D simulations, largely because they render localized 3D, rather than slab-symmetric 2D convective updrafts. The updrafts in the 3D simulations are stronger and more erect, but the general system properties of the 3D and 2D systems are still quite similar to one another.

Eventually, for each updraft cycle there is a point of cutoff when inflowing air parcels experience downward accelerations owing to hydrometeor loading as they approach the updraft. Thereafter, a suppressed phase ensues in which inflowing air cannot attain its LFC above the outflow boundary owing to negative buoyancy. The production of a strong downdraft then intensifies the surface outflow and thereby sets the stage for the next convective cycle. So long as the mesoscale pressure field remains in its quasi-stable configuration, this process occurs periodically and comprises an FFLS multicellular convective system. Owing to this precipitation cutoff mechanism, the period for the multicellular oscillations appears to be largely determined by the time required for convective cells to produce precipitation and downdrafts. The period in the simulated FFLS systems was typically about 13–16 min, but was occasionally delayed by longer suppressed phases.

This study represents a first attempt to understand the basic dynamics of convective lines with leading precipitation. Future work with high-resolution data and more sophisticated numerical simulations will help in further evaluating and expanding on these conclusions. In Part II of this paper, we go on to discuss the sensitivities of simulated FFLS systems to their environments and to other settings in the model, discuss their evolution, and explain a mechanism whereby such systems can be maintained despite inflow that passes through their preline precipitation.

*Acknowledgments.* The authors gratefully acknowledge the suggestions and contributions of M. Moncrieff and M. Weisman of the National Center for Atmospheric Research (NCAR), R. Fovell of UCLA, as well as the assistance of J. Knievel of Colorado State University (CSU) and NCAR, S. Tulich of CSU, and Z. Eitzen of CSU and the National Aeronautics and Space Administration. We also thank G. Cordova and R. Taft of CSU for their help throughout this work. The simulations in this study were made using the Advanced Regional Prediction System (ARPS) developed by the Center for Analysis and Prediction of Storms (CAPS), University of Oklahoma. CAPS is supported by the National Science Foundation (NSF) and the Federal Aviation Administration through combined Grant ATM92-20009.

NCAR provided supercomputer facilities and computational time for many of the simulations in this study, and D. Valent of NCAR's Scientific Computing Division was instrumental in helping us to exploit these resources. NSF funded this research under Grant ATM-0071371.

## REFERENCES

- Cai, H., and R. M. Wakimoto, 2001: Retrieved pressure field and its influence on the propagation of a supercell thunderstorm. *Mon. Wea. Rev.*, **129**, 2695–2713.
- Doswell, C. A., III, H. E. Brooks, and R. A. Maddox, 1996: Flash flood forecasting: An ingredients-based methodology. *Wea. Forecasting*, **11**, 560–581.
- Dudhia, J., M. W. Moncrieff, and D. W. K. So, 1987: The two-dimensional dynamics of West African squall lines. *Quart. J. Roy. Meteor. Soc.*, **113**, 121–146.
- Fankhauser, J. C., G. M. Barnes, and M. A. LeMone, 1992: Structure of a midlatitude squall line formed in strong unidirectional shear. *Mon. Wea. Rev.*, **120**, 237–260.
- Fovell, R. G., and Y. Ogura, 1988: Numerical simulation of a midlatitude squall line in two dimensions. *J. Atmos. Sci.*, **45**, 3846–3879.
- , and —, 1989: Effect of vertical wind shear on numerically simulated multicell storm structure. *J. Atmos. Sci.*, **46**, 3144–3176.
- , and P. S. Dailey, 1995: The temporal behavior of numerically simulated multicell-type storms. Part I: Modes of behavior. *J. Atmos. Sci.*, **52**, 2073–2095.
- , and P.-H. Tan, 1998: The temporal behavior of numerically simulated multicell-type storms. Part II: The convective cell life cycle and cell regeneration. *Mon. Wea. Rev.*, **126**, 551–577.
- Fritsch, J. M., R. J. Kane, and C. R. Chelius, 1986: The contribution of mesoscale convective weather systems to the warm-season precipitation in the United States. *J. Climate Appl. Meteor.*, **25**, 1333–1345.
- Grady, R. L., and J. Verlinde, 1997: Triple-Doppler analysis of a discretely propagating, long-lived, High Plains squall line. *J. Atmos. Sci.*, **54**, 2729–2748.
- Hane, C. E., 1973: The squall line thunderstorm: Numerical experimentation. *J. Atmos. Sci.*, **30**, 1672–1690.
- Houze, R. A., Jr., and E. N. Rappaport, 1984: Air motions and precipitation structure of an early summer squall line over the eastern tropical Atlantic. *J. Atmos. Sci.*, **41**, 553–574.
- Kessinger, C. J., P. S. Ray, and C. E. Hane, 1987: The Oklahoma squall line of 19 May 1977. Part I: A multiple Doppler analysis of convective and stratiform structure. *J. Atmos. Sci.*, **44**, 2840–2864.
- Klemp, J. B., 1987: Dynamics of tornadic thunderstorms. *Annu. Rev. Fluid Mech.*, **19**, 369–402.
- Lin, Y.-L., and L. E. Joyce, 2001: A further study of the mechanisms of cell regeneration, propagation, and development within two-dimensional multicell storms. *J. Atmos. Sci.*, **58**, 2957–2988.
- , R. L. Deal, and M. S. Kulie, 1998: Mechanisms of cell regeneration, development, and propagation within a two-dimensional multicell storm. *J. Atmos. Sci.*, **55**, 1867–1886.
- Nachamkin, J. E., R. L. McAnelly, and W. R. Cotton, 2000: Interactions between a developing mesoscale convective system and its environment. Part I: Observational analysis. *Mon. Wea. Rev.*, **128**, 1205–1224.
- Newton, C. W., and J. C. Fankhauser, 1964: On the movements of convective storms, with emphasis on size discrimination in relation to water-budget requirements. *J. Appl. Meteor.*, **3**, 651–668.
- Nicholls, M. E., R. H. Johnson, and W. R. Cotton, 1988: The sensitivity of two-dimensional simulations of tropical squall lines to environmental profiles. *J. Atmos. Sci.*, **45**, 3625–3649.
- Parker, M. D., and R. H. Johnson, 2000: Organizational modes of midlatitude mesoscale convective systems. *Mon. Wea. Rev.*, **128**, 3413–3436.
- , and —, 2004a: Simulated convective lines with leading precipitation. Part II: Evolution and maintenance. *J. Atmos. Sci.*, **61**, 1656–1673.
- , and —, 2004b: Structures and dynamics of quasi-2D mesoscale convective systems. *J. Atmos. Sci.*, **61**, 545–567.
- Rotunno, R., and J. B. Klemp, 1982: The influence of the shear-induced pressure gradient on thunderstorm motion. *Mon. Wea. Rev.*, **110**, 136–151.
- , —, and M. L. Weisman, 1988: A theory for strong, long-lived squall lines. *J. Atmos. Sci.*, **45**, 463–485.
- Schlesinger, R. E., 1980: A three-dimensional numerical model of an isolated thunderstorm. Part II: Dynamics of updraft splitting and mesovortex couplet evolution. *J. Atmos. Sci.*, **37**, 395–420.
- , 1984: Effects of the perturbation pressure field in numerical models of unidirectionally sheared thunderstorm convection: Two versus three dimensions. *J. Atmos. Sci.*, **41**, 1571–1587.
- Schultz, D. M., and R. J. Trapp, 2003: Nonclassical cold-frontal structure caused by dry subcloud air in northern Utah during the Intermountain Precipitation Experiment (IPEX). *Mon. Wea. Rev.*, **131**, 2222–2246.
- Seitter, K. L., and H.-L. Kuo, 1983: The dynamical structure of squall-line type thunderstorms. *J. Atmos. Sci.*, **40**, 2831–2854.
- Soong, S.-T., and Y. Ogura, 1973: A comparison between axisymmetric and slab-symmetric cumulus cloud models. *J. Atmos. Sci.*, **30**, 879–893.
- Szeto, K. K., and H.-R. Cho, 1994: A numerical investigation of squall lines. Part II: The mechanics of evolution. *J. Atmos. Sci.*, **51**, 425–433.
- Thorpe, A. J., M. J. Miller, and M. W. Moncrieff, 1982: Two-dimensional convection in non-constant shear: A model of midlatitude squall lines. *Quart. J. Roy. Meteor. Soc.*, **108**, 739–762.
- Weisman, M. L., J. B. Klemp, and R. Rotunno, 1988: Structure and evolution of numerically simulated squall lines. *J. Atmos. Sci.*, **45**, 1990–2013.
- Wilhelmson, R. B., and Y. Ogura, 1972: The pressure perturbation and the numerical modeling of a cloud. *J. Atmos. Sci.*, **29**, 1295–1307.
- Xue, M., K. K. Droegemeier, V. Wong, A. Shapiro, and K. Brewster, 1995: *Advanced Regional Prediction System Version 4.0 Users Guide*. Center for the Analysis and Prediction of Storms, Norman, Oklahoma, 380 pp. [Available from ARPS Model Development Group, CAPS, University of Oklahoma, 100 East Boyd, Norman, OK 73019-0628.]
- , —, and —, 2000: The Advanced Regional Prediction System (ARPS)—A multiscale nonhydrostatic atmospheric simulation and prediction tool. Part I: Model dynamics and verification. *Meteor. Atmos. Phys.*, **75**, 161–193.
- , and Coauthors, 2001: The Advanced Regional Prediction System (ARPS)—A multiscale nonhydrostatic atmospheric simulation and prediction tool. Part II: Model physics and applications. *Meteor. Atmos. Phys.*, **76**, 134–165.
- Yang, M.-J., and R. A. Houze Jr., 1995: Multicell squall-line structure as a manifestation of vertically trapped gravity waves. *Mon. Wea. Rev.*, **123**, 641–661.
- Yau, M. K., 1979: Perturbation pressure and cumulus convection. *J. Atmos. Sci.*, **36**, 690–694.